

The *JWST* Emission Line Survey (JELS): Extending rest-optical narrow-band emission line selection into the Epoch of Reionization

K. J. Duncan,^{1*} D. J. McLeod,¹ P. N. Best,¹ C. A. Pirie,¹ M. Clausen,¹ R. K. Cochrane,^{1,2} J. S. Dunlop,¹ S. R. Flury,¹ J. E. Geach,³ N. A. Grogin,⁴ C. L. Hale,^{5,1} E. Ibar⁶, R. Kondapally,¹ Zefeng Li,⁷ J. Matthee,⁸ R. J. McLure,¹ Luis Ossa-Fuentes⁵, A. L. Patrick,¹ Ian Smail,⁷ D. Sobral,^{9,10} H. M. O. Stephenson,¹¹ J. P. Stott,¹¹ and A. M. Swinbank⁷

¹*Institute for Astronomy, University of Edinburgh Royal Observatory, Blackford Hill, Edinburgh, EH9 3HJ, UK*

²*Department of Astronomy, Columbia University, New York, NY 10027, USA*

³*Centre for Astrophysics Research, School of Physics, Engineering and Computer Science, University of Hertfordshire, Hatfield, UK*

⁴*Space Telescope Science Institute, 3700 San Martin Drive, Baltimore, MD 21218, USA*

⁵*Astrophysics, Department of Physics, University of Oxford, Denys Wilkinson Building, Keble Road, Oxford, OX1 3RH, UK*

⁶*Instituto de Física y Astronomía, Universidad de Valparaíso, Avda. Gran Bretaña 1111, Valparaíso, Chile*

⁷*Centre for Extragalactic Astronomy, Department of Physics, Durham University, South Road, Durham DH1 3LE, UK*

⁸*Institute of Science and Technology Austria (ISTA), Am Campus 1, 3400 Klosterneuburg, Austria*

⁹*Departamento de Física, Faculdade de Ciências, Universidade de Lisboa, Edifício C8, Campo Grande, PT1749-016 Lisbon, Portugal*

¹⁰*BNP Paribas Corporate & Institutional Banking, Torre Ocidente Rua Galileu Galilei, 1500-392 Lisbon, Portugal*

¹¹*Department of Physics, Lancaster University, Lancaster LA1 4YB, UK*

Accepted XXX. Received YYY; in original form 11 October 2024

ABSTRACT

We present the *JWST* Emission Line Survey (JELS), a Cycle 1 *JWST* imaging programme exploiting the wavelength coverage and sensitivity of the Near-infrared Camera (NIRCam) to extend narrow-band rest-optical emission line selection into the epoch of reionization (EoR) for the first time, and to enable unique studies of the resolved ionised gas morphology in individual galaxies across cosmic history. The primary JELS observations comprise $\sim 4.7\mu\text{m}$ narrow-band imaging over $\sim 63\text{ arcmin}^2$ designed to enable selection of $\text{H}\alpha$ emitters at $z \sim 6.1$, as well as the selection of a host of novel emission-line samples including $[\text{O III}]$ at $z \sim 8.3$ and Paschen α/β at $z \sim 1.5/2.8$. For the prime F466N and F470N narrow-band observations, the emission-line sensitivities achieved are up to $\sim 2\times$ more sensitive than current slitless spectroscopy surveys (5σ limits of $1.1\text{--}1.6\times 10^{-18}\text{ erg s}^{-1}\text{cm}^{-2}$), corresponding to unobscured $\text{H}\alpha$ star-formation rates (SFRs) of $1\text{--}1.6\text{ M}_\odot\text{ yr}^{-1}$ at $z \sim 6.1$ and extending emission-line selections in the EoR to fainter populations. Simultaneously, JELS also obtained F200W broadband and F212N narrow-band imaging ($\text{H}\alpha$ at $z \sim 2.23$) that probes SFRs $\gtrsim 5\times$ fainter than previous ground-based narrow-band studies ($\sim 0.2\text{ M}_\odot\text{ yr}^{-1}$), offering an unprecedented resolved view of star formation at cosmic noon. In this paper we describe the detailed JELS survey design, key data processing steps specific to the survey observations, and demonstrate the exceptional data quality and imaging sensitivity achieved. We then summarise the key scientific goals of JELS and present some early science results, including examples of spectroscopically confirmed $\text{H}\alpha$ and $[\text{O III}]$ emitters discovered by JELS that illustrate the novel parameter space probed.

Key words: galaxies: evolution – galaxies: high-redshift – galaxies: emission lines – surveys – dark ages, reionization

1 INTRODUCTION

Since its launch, *JWST* has been delivering on its promise to transform our understanding of the earliest stages of galaxy formation, discovering a wealth of galaxies out to unprecedented redshifts (e.g. Robertson et al. 2024; Carniani et al. 2024), routinely providing spectroscopic confirmation of galaxies at $z > 10$ (e.g. Curtis-Lake et al. 2023; Arrabal Haro et al. 2023) and discovering new populations of active galactic nuclei (AGN, e.g. Labbe et al. 2023; Matthee

et al. 2023), whilst also beginning to reveal the detailed properties of the galaxies which powered the process of cosmic reionization (Sanders et al. 2023; Shapley et al. 2023). These early *JWST* results have demonstrated the potential to begin answering some of the key outstanding questions in extra-galactic astronomy: how and when do the first galaxies assemble? how does the chemical enrichment of the Universe proceed (Arellano-Córdova et al. 2022; Cameron et al. 2023; Curti et al. 2023; Isobe et al. 2023; Topping et al. 2024)? when do the first supermassive black holes (SMBHs) form (Labbe et al. 2023; Larson et al. 2023a; Maiolino et al. 2023; Greene et al. 2024; Matthee et al. 2024)? which galaxies drive the process of reioniza-

* E-mail: kdun@roe.ac.uk (KJD)

tion and what is its detailed topology (Tang et al. 2023; Umeda et al. 2024; Mascia et al. 2024; Witstok et al. 2024)?

However, to date, the majority of $z > 6$ galaxy samples confirmed by the *JWST* Near-Infrared Spectrograph (NIRSpec; Jakobsen et al. 2022) have typically been selected on the basis of broadband colours (de Graaff et al. 2024) or photometric redshift estimates (e.g. Bunker et al. 2023; Hu et al. 2024; Maseda et al. 2024). Such selections, however, can be limited by strong biases, with photometric redshift estimates highly dependent on prior assumptions on the UV continuum slopes and emission line properties (Arrabal Haro et al. 2023; Larson et al. 2023b). To constrain models of galaxy assembly and understand the processes driving early galaxy evolution (Somerville & Davé 2015; Yung et al. 2019), it is critical to study stellar mass or star-formation rate (SFR) selected samples of galaxies across cosmic time that are as complete and unbiased as possible (and where any remaining biases can be easily modelled).

The increasing strength of optical emission lines at $z > 2$ has been observed extensively (Mármol-Queraltó et al. 2016; Khostovan et al. 2016; Reddy et al. 2018). This trend, along with the ubiquity of high equivalent width emission lines in $z > 5$ galaxies (e.g. De Barros et al. 2019) can therefore be used to our advantage, through the efficient selection of galaxies based on their rest-optical emission lines. Slitless spectroscopic surveys (Kashino et al. 2023; Oesch et al. 2023) have already showcased the scientific potential of emission-line-selected samples with the *JWST*. These surveys provide a powerful method to trace the evolution of star-forming galaxies and AGN throughout cosmic history (Matthee et al. 2023; Covelo-Paz et al. 2024; Meyer et al. 2024).

Complementary to the grism or slitless spectroscopic approach is the selection of emission-line galaxies using photometric narrow-band observations. Like slitless spectroscopy, a key advantage of narrow-band selection is that galaxies are selected on the strength of their emission lines, broadly representing a star-formation rate-selected sample. When compared to broadband photometric selections, narrow-band surveys also offer the advantage that the robustly selected samples lie within a narrow redshift range while minimising the complex selection effects and biases (e.g. source blending) of slitless samples. As such, in recent years deep ground-based narrow-band surveys in the optical and near-IR have enabled measurements of the $H\alpha$ luminosity function out to $z \sim 2.2$ (Geach et al. 2008; Sobral et al. 2013; Matthee et al. 2017), providing robust measurements of the cosmic star-formation rate density, and enabled detailed studies of the morphology (Sobral et al. 2009, 2016), clustering (Sobral et al. 2010; Geach et al. 2012; Cochrane et al. 2017, 2018) and environment (Sobral et al. 2011) of star-forming galaxies. Finally, narrow-band selections also offer the advantage of providing a direct resolved view of the ionised gas in individual galaxies. Previous narrow-band studies have also provided the samples for high-resolution follow-up observations that enable more detailed morphological, chemical and dynamical studies (e.g. Swinbank et al. 2012; Stott et al. 2014; Cheng et al. 2020; Cochrane et al. 2021).

With the inclusion of narrow-band filters on the Near-Infrared Camera (NIRCam; Rieke et al. 2005, 2023) from $1.645\mu\text{m}$ all the way out to $4.7\mu\text{m}$, *JWST* now offers the potential for narrow-band selection of key optical emission lines such as $H\alpha$ and $[\text{O III}]$ out into the epoch of reionization (EoR; $z \sim 6.1$ and 8.3 respectively). Simultaneously, the longest wavelength NIRCam narrow-bands can also probe emission lines such as $\text{Pa}\alpha$ and $\text{Pa}\beta$ that were previously largely inaccessible in galaxies at the peak of cosmic star-formation history ($1 \lesssim z \lesssim 3$). The short wavelength ($< 2.5\mu\text{m}$) narrow-band filters, while not breaking new redshift ground, can exploit *JWST*'s exceptional resolution and sensitivity to constrain the detailed mor-

phology of ionised gas in galaxies at cosmic noon while also probing substantially fainter populations than previously possible from the ground (e.g. Geach et al. 2008; Sobral et al. 2013; Matthee et al. 2017).

The *JWST* Emission Line Survey (JELS; GO #2321, PI: Best) is a Cycle 1 NIRCam imaging programme designed to explore this new discovery space using narrow-band observations to detect and study emission-line galaxies across cosmic time. JELS leverages the extraordinary wavelength coverage, spatial resolution, and sensitivity of *JWST*/NIRCam to extend narrow-band galaxy selections into previously inaccessible observational regimes. Specifically, using F466N/F470N filters at $\sim 4.7\mu\text{m}$, the primary goal of JELS is to provide a clean $H\alpha$ emission selected sample of galaxies in the EoR ($z = 6.1$) that provides complementary constraints on the cosmic star-formation history and whose properties can be characterised and compared against UV-selected samples (Pirie et al. 2024). Simultaneous $2.12\mu\text{m}$ (F212N) narrow-band imaging is designed to probe a factor of ~ 5 deeper than previous ground based studies of $H\alpha$ at $z \sim 2$ (e.g. Sobral et al. 2012), doing so with sub-kpc resolution to reveal the distribution in star forming galaxies at the peak of cosmic star formation activity in unprecedented detail. In this paper, we present an overview of JELS; outlining the survey design, the *JWST*/NIRCam observations, the corresponding data processing and resulting properties. We then summarise the broader scientific goals of the survey, with illustrations of the unique statistical and resolved studies it enables.

The rest of this paper is set out as follows. In Section 2 we present the technical design of the JELS survey, the data reduction process and the photometric properties of the JELS imaging. In Section 3, we outline the scientific goals of JELS and the expected scientific returns. In Section 4, we present results from a sample of JELS $H\alpha$ and $[\text{O III}]\lambda 5008$ emission-line candidates confirmed by spectroscopic follow-up observations. Section 5 then summarises our conclusions. Throughout this paper, all magnitudes are quoted in the AB system (Oke & Gunn 1983) unless otherwise stated. We also assume a Λ Cold Dark Matter (Λ CDM) cosmology with $H_0 = 70 \text{ km s}^{-1} \text{ Mpc}^{-1}$, $\Omega_m = 0.3$ and $\Omega_\Lambda = 0.7$.

2 SURVEY OVERVIEW

The overall observing strategy and survey design of JELS was driven by requirements of the primary science case: firstly, to probe sufficient cosmological volume to detect a statistical sample of $z > 6$ $H\alpha$ emitters (a prediction of 40–60 based on conversion from the UV luminosity function), and secondly to probe significantly below the break of the luminosity function for $H\alpha$ emitters at $z > 6$, thus identifying ‘typical’ star-forming galaxies comparable to those selected in Lyman-break selected samples but with a highly complementary selection function.

While designed to be scientifically viable with only existing legacy multi-wavelength observations (e.g. CANDELS COSMOS; Grogin et al. 2011; Koekemoer et al. 2011), JELS was designed in tandem with the *JWST* Cycle 1 Guest Observer Treasury Program ‘Public Release Imaging For Extragalactic Research’ Survey (PRIMER; PI Dunlop, GO #1837). The complementary broadband observations across the full NIRCam wavelength range from PRIMER enable narrow-band excess selection at $\sim 4.7\mu\text{m}$ (see below), and are critical for panchromatic spectral energy distribution modelling and robust emission-line disambiguation for line emitters selected at both $2.12\mu\text{m}$ and $\sim 4.7\mu\text{m}$. An additional survey design criteria was therefore for the narrow-band imaging to be located entirely within

both the pre-existing deep optical and contemporaneous PRIMER NIRCcam observations.

2.1 Survey design

In the NIRCcam long-wavelength (LW) channels, JELS employs the closely-separated F466N and F470N narrow-band filters, with pivot wavelengths of 4.654 and 4.707 μm respectively (and effective filter widths, W_{eff} , of 0.535 and 0.510 μm). Either through difference imaging between the adjacent F466N/F470N bands, or narrow-band excess selection with respect to the F444W broadband imaging provided by the PRIMER COSMOS observations, line emitters can be selected in both filters and enable selection of $H\alpha$ emitters in two overlapping volumes centred at $z \sim 6.09$ and $z \sim 6.17$ (see Fig. 1).

Simultaneously, in the NIRCcam short-wavelength (SW) channels, JELS employs the F212N narrow ($\lambda_{\text{pivot}} = 2.12\mu\text{m}$, $W_{\text{eff}} = 0.027\mu\text{m}$) and F200W broadband ($\lambda_{\text{pivot}} = 1.99\mu\text{m}$, $W_{\text{eff}} = 0.419\mu\text{m}$) filters with a traditional narrow-broadband approach (Fig. 1). The F212N filter probes $H\alpha$ at $z = 2.23$, corresponding to the peak epoch of cosmic star formation, significantly extending the luminosity range of existing ground-based studies at this key redshift while also enabling resolved studies of the ionised gas at sub-kpc resolution. Besides ensuring matched broadband coverage for F212N narrow-band selection, the F200W broadband imaging also adds 2 – 3 \times the PRIMER exposure times within the centre of the field, providing significant gains in sensitivity for broader galaxy evolution studies in this critical legacy field.

JELS uses a 3 \times 3 mosaic strategy with 5 per cent overlap in each row and 57 per cent overlap between each column. We also adopt the standard 3-point intra-module dithering at each location to fill in short-band intra-chip gaps and account for both bad pixels and cosmic rays, with sub-pixel shifts at each primary dither position. The full JELS mosaic provides contiguous coverage over a total area of $\sim 63 \text{ arcmin}^2$. Combining the wavelength coverage of both F466N and F470N, this area corresponds to a $H\alpha$ selection volume of $\sim 2.4 \times 10^4 \text{ Mpc}^3$. For F212N, the single narrower filter results in an approximate $H\alpha$ selection comoving volume of $\sim 0.9 \times 10^4 \text{ Mpc}^3$.

For the NIRCcam SW and LW filter pairs, all observations use the MEDIUM-10 readout strategy, with 6 total integrations/dithers at each mosaic position. The F212N and F470N(+F444W)¹ filter combination was observed with 10 groups per integration, with this observing setup resulting in an on-sky integration time of 6313s over the full mosaic. Over the central ~ 40 per cent of the mosaic that is imaged twice, the total exposure time reaches 12626s. The F200W and F466N(+F444W)¹ filter combination was observed with 9 groups per integration with the same number of total integrations and dithers, yielding a total on-sky integration time of 5669s over the full mosaic (11338s over the central 40 per cent). Note that the difference in groups per integration between F466N and F470N observations (9 versus 10) is a result of changes to the readout strategy from the initial proposal (DEEP-10 to MEDIUM-10) to reduce the impact of cosmic rays, and the additional overheads that resulted in. The F212N/F470N pairing was prioritised to maximise the sensitivity in F212N.

¹ Both F466N and F470N are observed with F444W as a blocking filter. We use ‘(+F444W)’ here to denote that.

2.2 Observations and image reduction

The initial JELS observations were acquired over the period of May 6 to May 27 2023. Of these observations, 13 of 18 visits were observed without issue. In five of the eighteen total visits of the JELS observations (one F200W+F466N, four F212N+F470N), the NIRCcam imaging was subject to unusually bright scattered light, or ‘wisps’, that resulted in features in *both* the SW and LW detectors.² Initial tests demonstrated that the LW wisps remained spatially invariant within the field of view and have approximately constant amplitude within a visit and could therefore be effectively removed as set out below.

However, unlike most common wisps, the scattered light in the impacted JELS SW images is both extremely bright and shows notable small-scale variation in morphology between exposures within a given visit. With the corresponding LW images also impacted, standard approaches to mitigate the scattered light are not viable (see e.g. Robotham et al. 2023). For the impacted F200W+F466N visit, the availability of the separate PRIMER F200W observations and the limited impact on F466N mean that the overall impact is negligible. However, for the four F212N+F470N visits where the F212N artefacts are not viable for the proposed scientific goals, these specific pointings have been re-scheduled for observations. The F212N analysis (and to a lesser degree F470N) presented below therefore does not represent the final expected JELS image quality and sensitivity.

2.2.1 Imaging pipeline

To ensure consistency with the key ancillary imaging in the field, all JELS imaging is processed through the Primer Enhanced NIRCcam Image Processing Library (PENCIL; Dunlop et al., in prep) software, an enhanced version of the JWST pipeline (version 1.10.2). This PENCIL pipeline includes additional routines for the removal of snowballs and standard wisp artefacts, correction for $1/f$ noise striping as well as background subtraction. The astrometry of the reduced images is tied to the Gaia DR3 (Gaia Collaboration et al. 2022) reference frame and stacked to a consistent pixel scale (0.03 arcsec \times 0.03 arcsec). Prior to the construction of the final mosaics, we also take additional steps to mitigate the impact of the non-standard wisp artefacts in the five impacted JELS visits.

2.2.2 Scattered light removal

For the affected LW images that drive the primary JELS science aims, subtraction of the wisps is possible, but requires a specific approach tuned to these observations. In NIRCcam observations impacted by the typical wisp scattered light patterns, the robust prior positions (and spatial extent) of real sources in the affected SW modules can be obtained from the corresponding unaffected LW module image (Robotham et al. 2023). For the severe wisps in JELS, this is not possible since the LW frames themselves are affected. Templates for the LW scattered light therefore must be derived directly from the observed data and make use of the fact that our observing strategy provides 3 intra-module dithers at each pointing.

The impacted frames are first processed through the initial PENCIL data reduction stages as above. A scattered light template for a given set of exposures is then generated as follows:

- (i) Compact sources within the image are identified, with source detection employing a small locally varying background (25×25

² See e.g. the JWST Known Issues

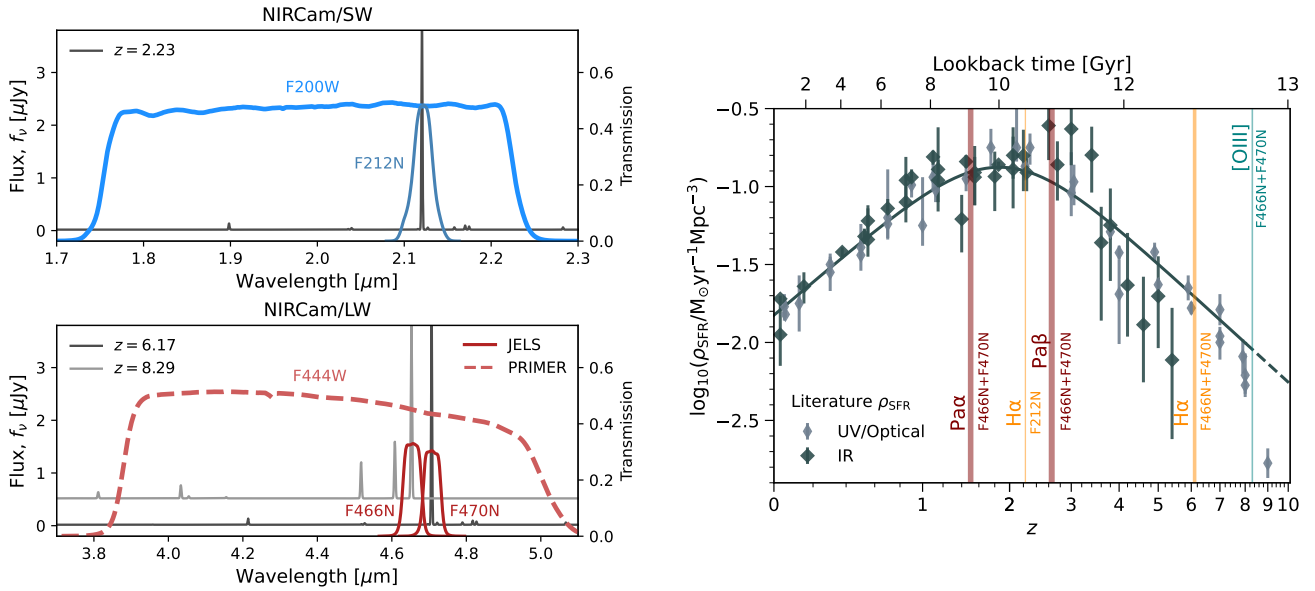


Figure 1. Left: Illustration of the JELS filter-set in the NIRC/SW (upper panel) and LW bands (lower panel). Shown for reference is an illustrative star-forming galaxy spectral energy distribution redshifted to key redshifts where the narrow-band filters probe $H\alpha$ ($z = 2.23$ for F212N, $z = 6.17$ for F470N) and $[OIII]\lambda 5008$ ($z = 8.29$ for F466N). The continuum flux density values are normalised arbitrarily for visualisation purposes. Right: Key emission lines and SFR-indicators probed by the JELS narrow-band filters in the context of the cosmic SFR density evolution. Literature UV/Optical (narrow diamonds) and infrared (wide diamonds) SFR density measurements are shown from the compilation by [Madau & Dickinson \(2014\)](#), see references therein) and illustrative additional measurements at $z > 3$ from recent studies in the rest-UV ([Bouwens et al. 2022](#)) and far-IR ([Dudzevičiūtė et al. 2020](#), for $850\mu\text{m}$ sources brighter than $> 0.2\text{mJy}$).

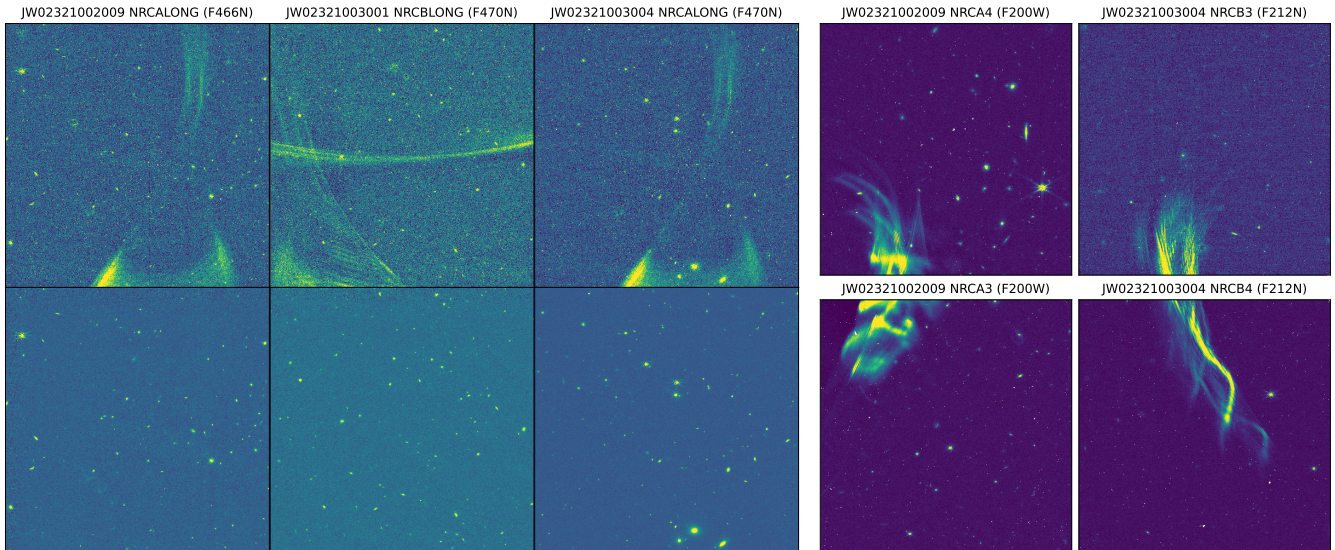


Figure 2. Left: Illustration of the transient scattered light and associated removal for the NIRC long wavelength imaging. The top row shows reduced individual frames for a single exposure in three of the F466N/F470N visits impacted by scattered light, labelled with the corresponding observation ID, NIRC module and filter. The bottom row shows the corresponding region of sky from the final mosaic after subtraction of the scattered light in individual frames and all overlapping dithers or mosaic visits have been combined. Each region (i.e. column) is shown with the same colour scale, with a linear stretch between 2 and 99.5 per cent of the individual impacted visit. Right: Illustration of the more extreme scattered light impacting the F200W and F212N observations.

pixel box-size) to select sources within regions of diffuse scattered light. In each exposure, the compact sources are then masked with additional dilation around each source.

(ii) The six frames are median stacked in the image plane to produce a wispy template for the frame. The median stacked template is then convolved with a Gaussian smoothing kernel with a full-width

half-maximum (FWHM) of 5 pixels to reduce small-scale noise (with interpolation for any remaining masked pixels).

(iii) A template mask is then generated by smoothing the scattered light template with a larger Gaussian kernel (FWHM = 25 pixels). Regions of the smoothed template image with flux below $0.5 \times \sigma_{\text{RMS}}$ are set to zero.

The final step is included to avoid the addition of noise from the generated template to pixels that are largely unaffected by the scattered light. By construction however, this leaves some areas of fainter diffuse scattered light present within individual frames prior to the final mosaicing and combination of all frames covering the region. Fig. 2 illustrates the effectiveness of the LW wisp removal on one of the impacted JELS visits.

Due to the extreme brightness and significant exposure-to-exposure variation in the spatial distribution within the affected SW frames, subtraction of the scattered light in SW is not feasible. However, even for the most severely impacted NIRCam SW modules, the majority of pixels in each frame remain perfectly usable for scientific analysis (see right panels of Fig. 2). For the preliminary JELS SW data reduction, we therefore follow a similar procedure as above, generating an average scattered light template for each affected module. The scattered light mask generated from template generation procedure outlined above is instead then used to mask the most severe areas of scattered light before the subsequent mosaicing.

Finally, once scattered light has been either subtracted or masked, the JELS imaging is then stacked onto the same 0.03 arcsec pixel grid as the PRIMER COSMOS imaging (see e.g. Donnan et al. 2024) that is tied to the same astrometric reference.

2.3 JELS Data Properties

Fig. 3 illustrates the relative position of the JELS imaging in the context of the PRIMER COSMOS field for the final observed position angles. With the exception of a small region in the south west of the field (the majority of which is covered by two or fewer dither positions), the JELS LW narrow-band imaging is fully contained within the NIRCam F444W broadband imaging necessary for optimal F466N/F470N emission-line selection. We estimate the local noise in the JELS imaging by placing down 0.3 arcsec diameter apertures in empty regions of the image, with the 1σ noise at a given sky position based on the scatter in the nearest 200 apertures. For a given limiting flux density in f_ν , we then estimate the corresponding maximum emission line sensitivity, $F_{\text{line}}(\text{erg s}^{-1}\text{cm}^{-2})$, assuming the flux density in the narrow-band is dominated by the emission line (i.e. ~ 0 continuum) or the uncertainty on the continuum estimate from the underlying broadband (F444W for F466N/F470N, F200W for F212N) is negligible. Note, this conversion also assumes the emission line is centred at the pivot wavelength, λ_{pivot} , of the narrow-band filter. Finally, the 0.3 arcsec aperture line flux limits are corrected to total fluxes for an assumed point-source based on the corresponding fraction of encircled energy for the respective point-spread function (PSF). The resulting distribution of limiting magnitudes and line fluxes for the F466N imaging is shown by the colour scale in Fig. 3 with the additional depth achieved in the central region of the field clearly visible.

2.3.1 F466N and F470N Narrow-band Sensitivity

To summarise the distribution of limiting line fluxes for the JELS narrow-band mosaics, in Fig. 4 we present the estimated line flux sensitivity as a function of both cumulative area (upper panel) and area per limiting flux ($\log_{10}(F_{\text{line}}/\text{erg s}^{-1}\text{cm}^{-2})$; lower panel). As designed, the F466N and F470N imaging reach comparable depths, with F470N reaching fractionally higher sensitivity over the field due to the additional group per integration and the additional depth of the central region is immediately apparent (e.g. lower panel of Fig. 4). To

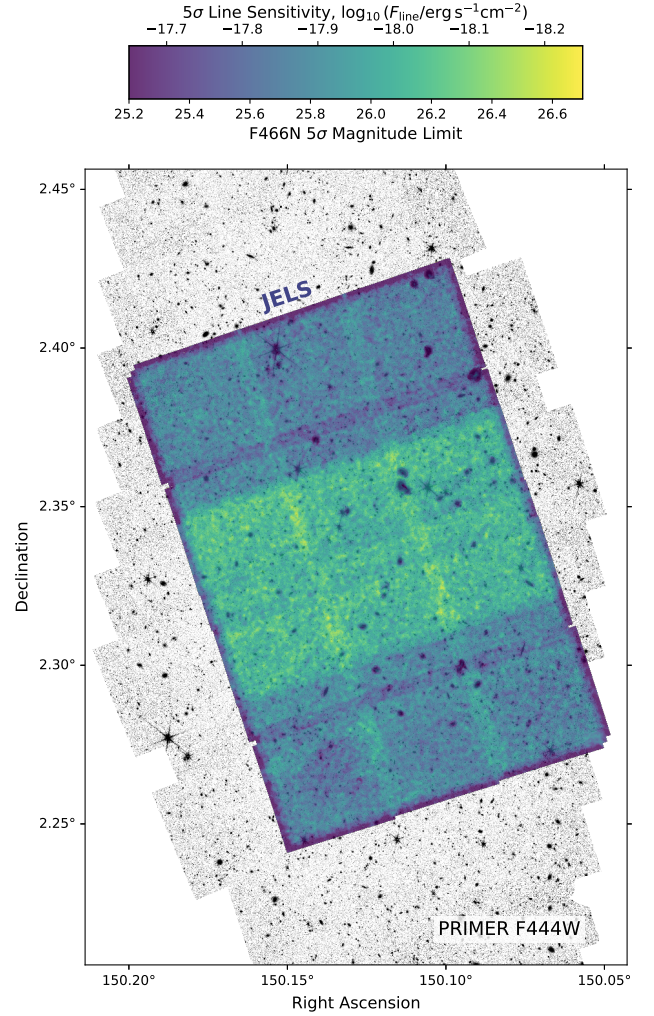


Figure 3. Illustration of the layout and sensitivity of the JELS narrow-band imaging within the PRIMER COSMOS field. The background image shows the PRIMER F444W broadband image with an illustrative image stretch. The 5σ limiting magnitude and corresponding maximum emission line sensitivity for the JELS F466N narrow-band imaging are shown by the colour scale, where the local noise at a given pixel is estimated from the nearest 200 0.3 arcsec apertures in empty sky regions. The central $\sim 1/3^{\text{rd}}$ of the JELS field that has double the exposure time is immediately apparent.

summarise the sensitivities reached in the central and overall field areas, Table 1 presents the limiting line flux sensitivities reached for the deepest 35 and 90 per cent of the field (see also the vertical dotted and dashed lines in Fig. 4) in each of the JELS narrow-bands. Also shown in Table 1 is the limiting *observed* $H\alpha$ luminosity, $L_{H\alpha}$, corresponding to the flux limit for the specified redshifts. The conversion to $H\alpha$ luminosity includes a correction for the typical expected contribution from $[\text{N II}]\lambda 6585$, assuming $\log_{10}([\text{N II}]\lambda 6585/H\alpha) = -1.31$ as measured for high- z galaxies in early *JWST* samples (Shapley et al. 2023), which leads to a 0.021 dex correction to $L_{H\alpha}$.

The measured sensitivity presented in Fig. 4 (and Table 1) compares to the pre-launch predicted sensitivity of $2.2 \times 10^{-18} \text{ erg s}^{-1}\text{cm}^{-2}$ within a 0.4 arcsec aperture (for an assumed characteristic radius of 0.15 arcsec and Sérsic $n = 1.2$ light-profile) for the areas with $\sim 6000\text{s}$ total exposure, extending down to $1.5 \times 10^{-18} \text{ erg s}^{-1}\text{cm}^{-2}$ over the central region with double the exposure time. Although formally not the exact same metric, the

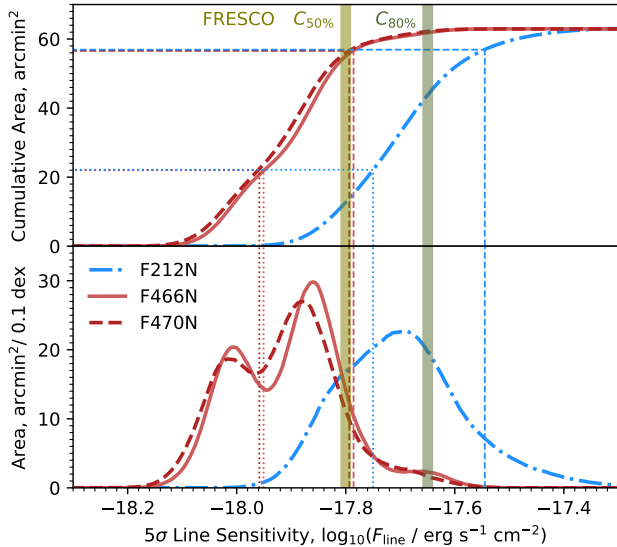


Figure 4. Emission line sensitivity of the JELS narrow-bands as a function of area covered, both cumulative area (top) and area per limiting sensitivity (bottom). The cumulative area corresponding to the deepest 35 per cent (~ 22 arcmin 2 ; i.e. the central region with double exposure) and 90 per cent (~ 57 arcmin 2) of the full JELS area are marked with thin horizontal dotted/dashed lines respectively, with vertical lines where they intersect the sensitivity curve. Exact values are tabulated in Table 1 alongside the corresponding $H\alpha$ luminosity limit. Also plotted for reference are the line fluxes corresponding to 50 and 80 per cent completeness derived for $H\alpha$ sources at $4.9 < z < 6.6$ in the FRESCO slitless spectroscopy survey (thick vertical lines; Covelo-Paz et al. 2024).

measured luminosity limits are between $\sim 0.2 - 0.3$ dex more sensitive than pre-launch predictions, in line with in-flight performance for NIRCcam photometry seen more widely in medium and broadband imaging (Rigby et al. 2023).

The limiting $L_{H\alpha}$ corresponds to *unobscured* $H\alpha$ star-formation rates of $2.7-4 M_{\odot} \text{ yr}^{-1}$ based on low-redshift calibrations (Hao et al. 2011), or $1-1.6 M_{\odot} \text{ yr}^{-1}$ for SFR calibrations more appropriate for younger stellar populations at higher redshift ($\log_{10}(L_{H\alpha}/M_{\odot} \text{ yr}^{-1}) = -41.64$; Theios et al. 2019). We note that the intrinsic $H\alpha$ luminosity distribution probed, once corrected for dust attenuation, will naturally be brighter. For example, Covelo-Paz et al. (2024) measure an average extinction of $A_{H\alpha} = 0.47$ for $4 < z < 6.5$ $H\alpha$ emitters.

Given the $\sim 4.7\mu\text{m}$ sensitivities achieved over the survey area of ~ 63 arcmin 2 , the JELS narrow-band survey probes a complementary parameter space to the "First Reionization Epoch Spectroscopically Complete Observations" (FRESCO; GO #1895, Oesch et al. 2023) slitless spectroscopy survey, which reaches a 5σ line sensitivity at $\sim 4-5\mu\text{m}$ of $2 \times 10^{-18} \text{ erg s}^{-1} \text{ cm}^{-2}$ (see also Covelo-Paz et al. 2024, as shown in Fig. 4). Covering two ~ 62 arcmin 2 fields (of which $4.4-5\mu\text{m}$ is visible over ~ 73 per cent), the wavelength coverage of FRESCO allows un-targeted detection of emission-line sources over a wider redshift range and hence survey volume (plus simultaneous spectroscopic confirmation). In contrast, the JELS narrow-band is sensitive to fainter line fluxes at $\sim 4.7\mu\text{m}$ over the full mosaic, reaching up to $\sim 2\times$ fainter in the central region, with no losses due to dispersion off the detector or significant blending or contamination from bright sources. As such, JELS is able to robustly detect a sample of $H\alpha$ emitters at $z > 6$ comparable to both FRESCO fields combined, despite the limited volume ($z \sim 6.1$ vs $6 < z < 6.6$, see Section 3.1.1

Table 1. Limiting emission line flux and corresponding $L_{H\alpha}$ sensitivity reached for the three JELS narrow-band images shown in Fig. 4, with limits corresponding to the deepest 35 per cent of the field (~ 22 arcmin 2 ; i.e. the central region with double exposure) and the deepest 90 per cent (~ 57 arcmin 2).

Filter ($z_{H\alpha}$)	Flux Limit		Luminosity Limit	
	$\log_{10}(F_{\text{line}}/\text{erg s}^{-1} \text{ cm}^{-2})$		$\log_{10}(L_{H\alpha}/\text{erg s}^{-1})$	
Percentage of the JELS coverage				
	35%	90%	35%	90%
F212N (2.23)	-17.75	-17.54	40.85	41.05
F466N (6.09)	-17.95	-17.79	41.69	41.85
F470N (6.17)	-17.96	-17.79	41.69	41.86

below). Additionally, as further discussed in Section 3.2, the narrow-band imaging retains the full two-dimensional morphological information, providing information on the spatially resolved ionised gas structures of individual galaxies (cf. the ensemble structural information robustly measurable in slitless spectroscopy; Matharu et al. 2024).

2.3.2 F212N Narrow-band Sensitivity

For the F212N narrow-band, the preliminary mosaic reaches a 5σ limiting line flux of $2.9 \times 10^{-18} \text{ erg s}^{-1} \text{ cm}^{-2}$ for the deepest 90 per cent of the field (see Table 1). This depth corresponds to ~ 0.8 dex lower $H\alpha$ luminosities than probed at $z \sim 6.1$, reaching $L_{H\alpha} > 10^{41.05} \text{ erg s}^{-1}$ ($10^{40.85} \text{ erg s}^{-1}$ in the central doubly imaged area). For the same SFR calibration assumed above (Theios et al. 2019), these limits correspond to unobscured $H\alpha$ SFRs of $0.16-0.26 M_{\odot} \text{ yr}^{-1}$. We note that in Fig. 4, the bi-modality corresponding to the central region is currently less clearly defined for the F212N filter due to the loss of exposure from scattered light masking and the increased impact of bright stars in the field (c.f. the extent of diffraction spikes in Fig 5 relative to Fig. 3). Nevertheless, the JELS imaging still reaches line sensitivities $\sim 5\times$ more sensitive than the previous state-of-the-art over the full field and almost an order of magnitude more sensitive in the central region (cf. $\sim 10^{41.7} \text{ erg s}^{-1}$; Geach et al. 2008; Hayes et al. 2010; Sobral et al. 2013). Once the visits severely impacted by scattered light have been re-observed, the overall noise properties of the complete F212N mosaic within the effected region are expected to significantly improve.

2.3.3 F200W Broadband Sensitivity

Finally, in Fig. 5, we illustrate the additional F200W broadband depth gained in the centre of the PRIMER COSMOS field from the addition of the JELS imaging. The F200W mosaic in COSMOS using only PRIMER imaging reaches an average global 5σ depth of $m_{F200W} = 28.3$ over the best 63 arcmin 2 of the field when the depths are calculated using the same 0.3 arcsec apertures corrected to total flux (we note that the different depths quoted in Donnan et al. 2024 are calculated from PSF homogenised images). With the JELS F200W imaging included, the equivalent deepest area within the field reaches a median depth of $m_{F200W} = 28.7$.

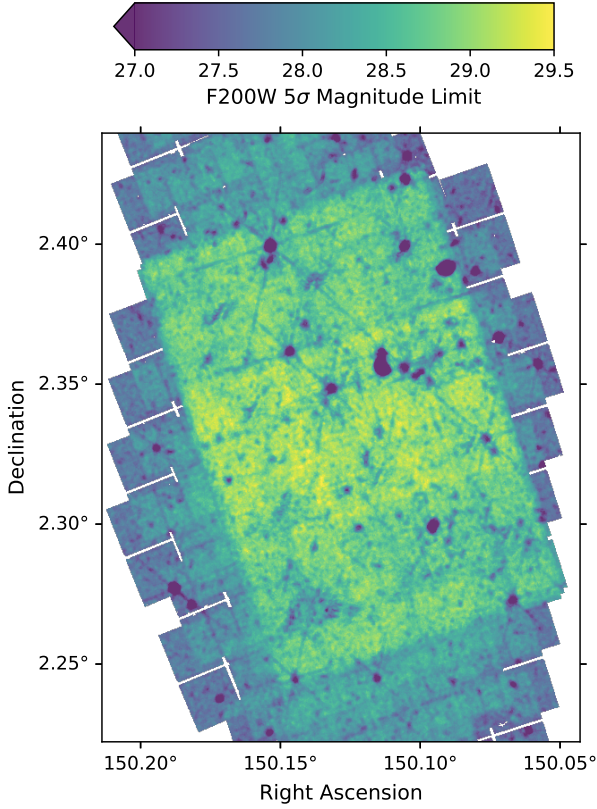


Figure 5. Illustration of sensitivity of the combined PRIMER and JELS F200W imaging in the COSMOS field. The 5σ limiting magnitude and corresponding maximum emission line sensitivity are shown by the colour scale, where the local noise at a given pixel is estimated from the nearest 200 0.3 arcsec apertures in empty sky regions and corrected to total fluxes given the fraction of encircled energy for the F200W PSF.

3 SCIENTIFIC GOALS

3.1 Global line emitter properties

3.1.1 A census of $H\alpha$ emitters at $z \sim 6.1$

The primary goal of the JELS survey is to carry out the first narrow-band $H\alpha$ survey at $z > 6$, obtaining a sample of ≥ 40 $H\alpha$ emitters (Pirie et al. 2024). The JELS $H\alpha$ sample is designed to provide tight constraints on the faint end of the $H\alpha$ luminosity function at $z \sim 6$, with sufficient accuracy to constrain the space density of $H\alpha$ emitters at these luminosities to within 0.1 dex. In addition to providing new integral constraints on the cosmic star-formation rate density of galaxies in the EoR (Madau & Dickinson 2014, see Fig. 1), the JELS $z \sim 6.1$ $H\alpha$ sample will make it possible to study the nature of star-forming galaxies at this epoch in a relatively unbiased sample and to constrain the scaling relations linking ongoing star formation to key galaxy properties such as masses, sizes (Stephenson et al. *in prep*) and clustering properties (Hale et al., *in prep*).

To illustrate the complementarity between the JELS narrow-band and other slitless spectroscopy approaches, in Fig. 6 we show the distribution in redshift and emission-line flux for a sample of the 35 most robust F466N/F470N $H\alpha$ emitters (presented in Pirie et al. 2024), alongside the published sample of $H\alpha$ emitters detected in the FRESCO survey (Covelo-Paz et al. 2024). Given the high completeness within the survey volume and the range of line fluxes probed, the JELS $H\alpha$ sample also offers a valuable test-bed for understanding the

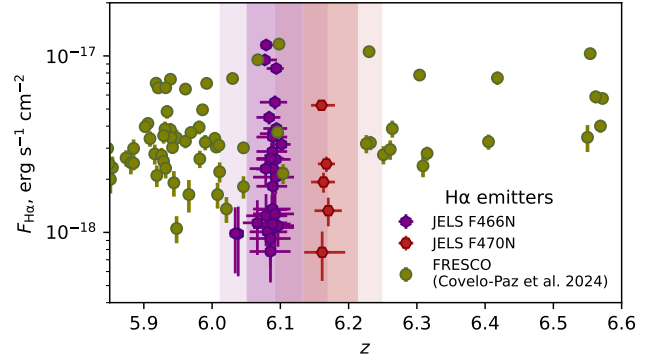


Figure 6. Illustration of the novel sample size and emission-line flux parameter space probed by the JELS $H\alpha$ selection compared to slitless spectroscopy samples in the literature. Filled hexagons show the photo- z and measured line flux for the robust $H\alpha$ samples ($F_{\text{line}}/\text{erg s}^{-1}\text{cm}^{-2}$; Pirie et al. 2024) selected in F466N and F470N. The FRESCO $H\alpha$ sample (Covelo-Paz et al. 2024) is shown for comparison. Light shaded regions correspond to the redshift range where $H\alpha$ falls within the minimum and maximum (> 1 per cent of peak filter throughput) wavelengths covered by F466N/F470N, with the darker shaded ranges illustrating the corresponding effective wavelength range.

potential biases and limitations of UV-based selection techniques that are ubiquitously used at high redshifts. For example, the bursty nature of star-formation in low mass galaxies is now understood to play a key role in dictating the observability of high-redshift galaxies (Sun et al. 2023a), and hence significantly impacting on the inferred UV luminosity functions (Sun et al. 2023b), as well as strongly impacting estimates of key galaxy properties such as stellar mass (Endsley et al. 2023) and ionising photon escape (Flury et al. 2024). With JELS, it is possible to derive the distribution of $H\alpha$ (~ 10 Myr time-scales) to UV star-formation rates (~ 100 Myr timescales) in a homogeneously selected sample of galaxies in the EoR for the first time. By selecting on emission-line strength, the narrow-band selection is naturally sensitive to the highest equivalent width population and hence provides constraints on the youngest or most extreme burst populations (see e.g. Maseda et al. 2023). Recent studies with *JWST* medium bands confirm the expectation that high-redshift galaxies displaying evidence for elevated recent star-formation activity are typically the most efficient ionising photon producers (i.e. higher ξ_{ion} ; Simmonds et al. 2024), while modelling predicts that very high $H\alpha$ SFRs could correlate with increased ISM porosity (Clarke & Oey 2002) and hence Lyman continuum photon escape. The high EW emission-line sources selected by JELS may therefore offer an especially valuable probe of the most extreme ionisers of the IGM.

Further enhancing the scientific potential of the JELS $H\alpha$ sample in this area is the ongoing deep Multi Unit Spectroscopic Explorer (MUSE; Bacon et al. 2010) integral field spectroscopy over the full JELS survey footprint (ESO Large Programme 112.25WM.001, PI: Swinbank), reaching triple the exposure time per pointing of the MUSE-Wide Survey (Urrutia et al. 2019) over $\sim 1.75\times$ greater area. The combination of a homogeneously selected $H\alpha$ sample with complete resolved rest-UV spectroscopy will enable a broad range of studies into the late stages of cosmic reionization, with the potential to improve on and complement existing studies of $\text{Ly}\alpha$ emitter fractions (Stark et al. 2010), $\text{Ly}\alpha$ emission-line profiles (Mason et al. 2018), constraints on ξ_{ion} as a function of $\text{Ly}\alpha$ properties (Prieto-Lyon et al. 2023; Saxena et al. 2024) and resolved studies of $\text{Ly}\alpha$ (e.g. Smith et al. 2018; Roy et al. 2023).

Another key advantage offered by narrow-band samples is that they

are ideally suited for clustering analyses, as the narrow redshift slice minimises redshift projection effects (cf. [Geach et al. 2012](#); [Cochrane et al. 2017](#)). Measurement of the correlation of $H\alpha$ emitters at $z \sim 6.1$ will enable constraints on the dark-matter halos hosting these star-forming galaxies. In addition to placing these sources into their broader cosmological context for direct comparisons with galaxy formation simulations, these measurements will offer another critical comparison against existing Lyman break and $Ly\alpha$ emitter galaxy samples at this epoch (see also Section 3.1.3).

3.1.2 The faint SF population at cosmic noon

One of the largest uncertainties in constraining the global cosmic SFR density is the precision to which the faint-end slope of respective LFs can be reliably constrained. The faint-end of the UV LF has been tightly constrained across the bulk of cosmic history (reaching $M_{UV} > -15$ out to $z > 6$; [Bhatwadekar et al. 2019](#); [Bouwens et al. 2022](#); [Harikane et al. 2022](#)), with very tight constraints at cosmic noon ([Parsa et al. 2016](#), $\alpha \pm 0.04$) and clear evidence of steepening slopes as redshift increases. Current constraints on the $H\alpha$ LF are however significantly more limited ([Sobral et al. 2012](#)). This is a critical measurement, since the difference between a faint-end slope of $\alpha = -1.75$ and $\alpha = -1.5$ corresponds to a factor-of-two difference in the integrated star-formation rate density.

The extreme depth of our *JWST* NIRC*am* imaging means that the JELS F212N observations will detect $H\alpha$ emitters $\sim 5\times$ fainter than previous ground-based studies, with an estimated sample size of ~ 200 . The resulting determination of the faint-end slope of the $z = 2.23$ $H\alpha$ luminosity function can achieve a precision of $\delta\alpha < 0.05$, almost $3\times$ better than current limits, thereby tightly constraining the relative evolution of dwarf galaxies. Furthermore, the extensive broadband imaging from HST/CANDELS and PRIMER will enable robust constraints on the stellar masses, star-formation histories and the dust attenuation of the $H\alpha$ sample.

In addition to the F212N $H\alpha$ sample constraints at $z = 2.23$, the JELS F466N/F470N filters also probe the Paschen lines $Pa\alpha$ and $Pa\beta$ at $z \sim 1.5$ and 2.6 respectively, bracketing the peak of cosmic star-formation (Fig. 1). Essentially unaffected by dust, the $Pa\alpha$ ($1.87\mu\text{m}$) and $Pa\beta$ ($1.28\mu\text{m}$)-lines offer unbiased instantaneous SFR-indicators ([Cléri et al. 2022](#)). For the JELS F466N limiting line flux (90th percentile), the corresponding $Pa\alpha$ and $Pa\beta$ luminosity limits reach $10^{40.36}$ and $10^{40.96}\text{erg s}^{-1}$ respectively (0.17 dex deeper in the central region). Assuming Case B recombination, a temperature of $10,000\text{K}$ and electron density, $N_e = 10^4\text{cm}^{-3}$, we expect line intensity ratios of $H\alpha/Pa\alpha = 8.584$ and $H\alpha/Pa\beta = 17.614$ ([Storey & Hummer 1995](#)). The Paschen line sensitivities at $z \sim 1.5$ ($Pa\alpha$) and 2.6 ($Pa\beta$) therefore correspond to equivalent $H\alpha$ luminosities of $10^{41.29}$ and $10^{42.2}\text{erg s}^{-1}$, or star-formation rates of 0.27 and $2.29 M_\odot\text{yr}^{-1}$ respectively³. We caveat that recent evidence suggests that the standard Case B assumption may not be valid in all galaxies, both in the lower redshift Universe ([Flury et al. 2022](#); [Scarlata et al. 2024](#)) and at the redshifts probed by the JELS Paschen samples ([Pirzkal et al. 2024](#)). The inferred limiting star-formation rates are therefore only illustrative. Statistical samples of bright Paschen line emitters at cosmic noon selected by JELS therefore also offer an ideal test-bed for future spectroscopic studies exploring the diversity of interstellar medium (ISM) conditions in star-forming galaxies through the distribution of Balmer and Paschen line ratios.

³ Where $\log_{10}(\text{SFR}_{H\alpha}/M_\odot\text{yr}^{-1}) = -41.64 + \log_{10}(L_{H\alpha}/\text{erg s}^{-1})$ assuming the SFR calibration of [Theios et al. \(2019\)](#).

3.1.3 The role of galaxies in reionization – [O III] emitters at $8.3 \lesssim z \lesssim 8.5$

Prior to *JWST*, the prevalence of high EW [O III] emitters at $z > 6$ had been studied in large samples based on strong broadband colour excess (e.g. [De Barros et al. 2019](#)), with the [O III]EW found to strongly correlate with redshift ([Khostovan et al. 2016](#)). Studies of the properties of [O III] emitters at $z > 6$ from medium/broadband *JWST* observations ([Simmonds et al. 2023](#)) and slitless spectroscopy ([Matthee et al. 2023](#)) indicate that the highest EW sources are likely to be producing ionizing photons with very high efficiency, and could therefore represent key drivers of the early stages of cosmic reionization. Similar to the $H\alpha$ selection, homogeneously selected samples of [O III] emission-line sources from JELS can therefore offer a probe of the earlier stages of reionization at $z \sim 8.4$, both through the overall statistical constraints and by sign-posting the sites of the largest ionised bubbles (e.g. [Witstok et al. 2024](#)).

When the [O III] $\lambda 5008$ line falls within F466N ($z = 8.298$ at λ_{pivot}), the narrow-band line flux limits presented in Table 1 correspond to luminosity limits of $L_{[\text{O III}]\lambda 5008} \sim 10^{41.97}\text{erg s}^{-1}$ for the deeper JELS region, increasing to $\sim 10^{42.14}\text{erg s}^{-1}$ for 90 per cent of the survey area. At slightly higher redshifts, the fainter [O III] $\lambda 4960$ line is also then redshifted into the narrow-bands (extending up to e.g. $z = 8.492$ at $\lambda_{\text{pivot,F470N}}$) with comparable measured line sensitivity. For an assumed intrinsic [O III] $\lambda 5008$ /[O III] $\lambda 4960$ ratio of 2.98 ([Storey & Zeppen 2000](#)), we note however the effective [O III] $\lambda 4960$ sensitivity is ~ 0.5 dex lower than for [O III] $\lambda 5008$ selection. The JELS narrow-band imaging is highly complementary to slitless spectroscopic surveys, extending emission-line selections to fainter $L_{[\text{O III}]\lambda 5008}$ at $z \sim 8$ ([Meyer et al. 2024](#)), improving constraints on the faint end of the [O III] $\lambda 5008$ LF and revealing key populations critical in the process of cosmic reionization. The full sample of JELS selected [O III] emitters will be presented in Duncan et al. (in prep), however below we illustrate the exquisite morphological information provided by the narrow-band imaging (Section 3.2) and the reliability and sensitivity of the selection (Section 4).

3.1.4 Other line emitter samples

Finally, while the science cases outlined above focus on intrinsically brighter emission-line species, the combination of high-sensitivity and extensive ancillary observations sufficient to distinguish between potential redshift solutions means that JELS is sensitive to a broad range of novel emission-line sources. Further examples range from the $3.3\mu\text{m}$ poly-aromatic hydrocarbon (PAH) feature at $z \sim 0.4$ (F466N/F470N) in the lower redshift Universe, to [S III] $\lambda 9069$ at $z \sim 4.1$ (F466N/F470N) and [O II] $\lambda 3727$ at $z \sim 4.7$ (F212N) in the early Universe. Sources with line strengths in intrinsically weaker optical–near-IR line species sufficiently bright to be robustly selected as excess sources in JELS likely represent ideal targets for detailed spectroscopic follow-up. Regardless, the ability to isolate emission lines in narrow-band filters results in improved photo- z and SED modelling precision for all such sources, as well as the potential for detailed morphological studies.

3.2 Spatially resolving ionised gas properties

Early *JWST* observations have demonstrated that the preceding picture where regular Hubble-sequence morphologies emerged around cosmic noon ($1 < z < 3$; [Mortlock et al. 2013](#)) may not be correct,

with discy morphologies potentially dominating the galaxy population as early as $z \sim 7$ (e.g. [Ferreira et al. 2022](#); [Kartaltepe et al. 2023](#); [Conselice et al. 2024](#)). Robustly measuring galaxy morphologies at $z > 2$ is crucial for far more than simple galaxy classification. Constraining the spatial distribution of on-going star-formation within galaxies as a function of stellar mass (and ideally halo mass), or other key properties such as AGN activity, can directly inform models of feedback in hydro-dynamical simulations ([Cochrane et al. 2023](#)). One of the key advantages offered by narrow-band emission-line selection over slitless spectroscopic surveys is immediate access to the robust 2D emission-line morphologies in *individual* galaxies. This means that JELS will enable studies of resolved ionised gas properties in less biased galaxy samples on sub-kpc scales without the need for complex forwarding modelling of multiple dispersion directions ([Pirzkal et al. 2018](#); [Estrada-Carpenter et al. 2024](#); [Shen et al. 2024](#)), or the stacking analysis of statistical samples ([Nelson et al. 2013](#); [Matharu et al. 2024](#); [Liu et al. 2024](#)).

As with integrated measurements above (Sections 3.1.1-3.1.4), this is particularly valuable when the ionised gas offers a direct SF tracer. The JELS $H\alpha$ and F466N/F470N $Pa\alpha/Pa\beta$ samples offer a clean probe of sub- L^* galaxies at their respective redshifts whose multi-wavelength properties, resolved structures and parametrised morphologies can be compared with those of brighter galaxies (and lower-redshift samples) to investigate the physical processes driving star formation within these galaxies (e.g. [Cochrane et al. 2021](#)). In Fig. 7 we show the rest-UV, ionised gas (narrow-band excess) and rest-optical/near-infrared continuum morphologies for examples of both F466N/F470N and F212N excess selected emission-line samples. The advantage of resolving both the UV and $H\alpha$ (or $Pa\alpha$) star formation is immediately evident, with significant variation both between the two star formation probes and the underlying continuum that gives insights into the star-formation properties of galaxies that cannot be obtained from one alone (e.g. the distribution of dust, or the variation of star-formation timescales within the galaxy). When extended to the full narrow-band samples, JELS can therefore constrain the morphology of on-going star formation compared to that of the in-situ stellar mass (measured from resolved SED fitting with full PRIMER observations) for a representative sample of SFGs, testing whether the inside-out growth of galaxies inferred from stacks at $z < 1.5$ ([Nelson et al. 2016](#)) is true for all individual galaxies and tracing this over a critical period in the morphological history of galaxies.

4 SPECTROSCOPICALLY CONFIRMED JELS EMITTERS

To further illustrate the diversity of galaxy properties present within the populations selected by JELS and the efficacy of the narrow-band selection, here we present spectroscopic confirmations of four high- z line emitters selected by JELS that were included as filler targets in the Director’s Discretionary program DD 6585 (PI: Coulter).

The JELS sample configured in the NIRSpec PRISM observations was selected from a F466N detected catalogue with $\text{SNR}_{F466N} > 5$ in 0.3 arcsec apertures. All sources satisfy emission-line excess criteria with colours $F444W - F466N > 0.3$ and $F470N - F466N > 0.15$ (corresponding to a rest-frame equivalent width of $\text{EW}_0 \gtrsim 20\text{\AA}$). Photometric redshifts (photo- z s) derived from PSF homogenised photometry from all available *HST*/ACS, *HST*/WFC3 and *JWST*/NIRCam filters identified all sources as secure high- z ($z > 5.5$) candidates⁴. Of

the four JELS emission-line candidates observed with NIRSpec, two are robustly identified as $H\alpha$ emitters with well constrained photo- z s at $z \sim 6.1$, with the other two robustly identified as $z \sim 8.3$ $[\text{O III}]\lambda 5008$ emitters.

In Fig. 8, we show a subset of the available HST and JWST/NIRCam cutouts for each object as well as the standard MAST pipeline reduced 2D and 1D PRISM spectra. Motivated by the expectation of high-EW emission-lines, we derive spectroscopic redshifts from the 1D PRISM spectra through a simple χ^2 -minimisation, fitting an emission-line template (convolved to the PRISM spectral resolution at $4.6\mu\text{m}$) to the continuum-subtracted spectrum over the wavelength range of $3 < \lambda < 5\mu\text{m}$ ⁵.

The two confirmed $H\alpha$ sources are shown in the top row of Fig 8, observed with exposure times of 5 909 and 17 725s respectively. JELS J100033.5+022355.5 (upper left panel) is representative of a large fraction of the $H\alpha$ emitters selected by JELS, with the overall spectral energy distribution (SED) dominated by high equivalent width (EW) emission lines. The high-EW emission-line contribution can be inferred from the photometry cutouts alone, with $[\text{O III}]$ and $H\beta$ responsible for the F356W broadband showing clearly elevated flux; this is confirmed by the PRISM spectroscopy. In comparison, JELS J100033.3+022331.7 (upper right panel) exhibits significant UV and optical continuum detections across the broadband SED, although F356W is still significantly enhanced relative to F277W. The corresponding PRISM spectrum reveals significantly lower EW emission-lines, with evidence for a more evolved stellar population in the form of a clear Balmer break.

The bottom row of Fig. 8 then presents the two $[\text{O III}]\lambda 5008$ emitters selected from JELS, both with total on-source exposure times of 11 817s. The left-hand source, J100021.3+022231.5, is securely identified as a $z \sim 8.3$ $[\text{O III}]\lambda 5008$ emitter by the photo- z analysis to a precision of $< 0.005 \times (1+z)$ despite having only weak constraints on the Lyman break and very faint rest-UV continuum. With $\text{SNR}_{F115W} < 1$ and $\text{SNR}_{F150W} < 4$ (in 0.3-arcsec diameter apertures), photo- z estimates using broadband photometry only are limited to constraining the source as $z \gtrsim 5$, but with a very broad posterior allowing solutions up to $z > 10$. Although faint, the extracted 1D PRISM spectrum for this source shows clear $H\beta$, $[\text{O III}]\lambda 4960$, $[\text{O III}]\lambda 5008$ and $[\text{O II}]\lambda 3727$ lines confirming the photo- z redshift solution. The right-hand source, J100025.4+022024.6, is selected as a narrow-band excess by JELS, but is also bright enough in the rest-UV to be robustly selected as $z \sim 8$ from broadband photometry (and was also included in the DD filler programme from an independent selection). The rest-UV continuum is detected in the NIRSpec PRISM observation (we limit the wavelength range of the PRISM spectra in Fig. 8 to $> 2.5\mu\text{m}$ to demonstrate the resolved $[\text{O III}]\lambda 4960$ and $[\text{O III}]\lambda 5008$ lines).

Although only a limited sample, the confirmation of all four narrow-band excess selected sources and their diverse properties gives evidence that JELS offers a broad and robust selection in novel parameter space. In addition to enabling unique science from the

three different template sets: the default `fsp`s set supplemented with the high- z templates of [Larson et al. \(2023b\)](#), the `sFHz` set supplemented with the obscured AGN template of [Killi et al. \(2023\)](#) and the `eazy_v1.3` set. The consensus photo- z s combining all three estimates are derived following the procedure outlined in [Duncan et al. \(2019\)](#). See [Pirrie et al. \(2024\)](#) for full details.

⁵ Our derived spectroscopic redshifts are all in agreement with the independently derived estimates from the DAWN JWST Archive: https://s3.amazonaws.com/msaexp-nirspec/extractions/nirspec_graded_v3.html.

⁴ The photo- z s were estimated using EAzy ([Brammer et al. 2008](#)) with

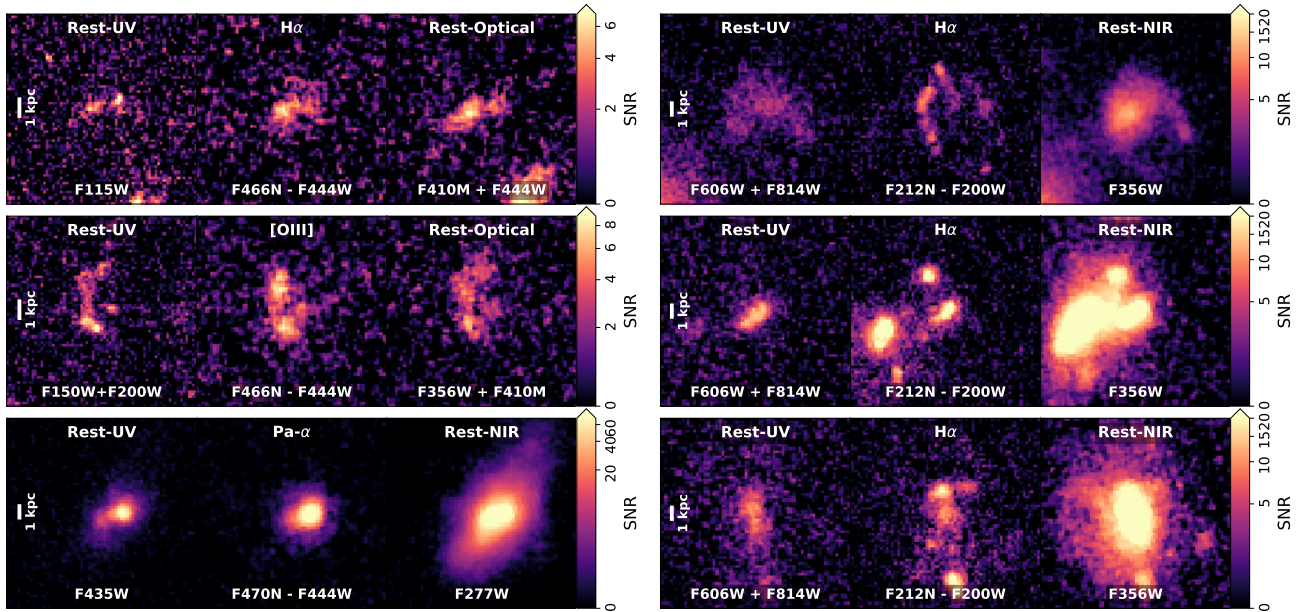


Figure 7. Illustration of resolved rest-UV (left), emission-line (centre) and rest-frame optical/NIR (right) for $H\alpha$, $[O\text{ III}]$ and $\text{Pa}\alpha$ emission line objects in JELS. Examples of F466N or F470N selected sources are shown in the left column, with examples of bright extended F212N excess sources shown in the right column. The corresponding broad and narrow-band filter combinations are indicated in each image. Cutouts are $2\text{ arcsec} \times 2\text{ arcsec}$ in size, with consistent colour scales illustrated by the corresponding colour bar and 1 proper kiloparsec at the corresponding redshift shown for reference.

photometric data alone, the JELS emission-line samples are therefore ideal for future spectroscopic studies.

5 SUMMARY

We have presented an overview of the *JWST* Emission Line Survey (JELS), a *JWST* imaging survey designed to extend selection of emission-line galaxies using narrow-band filters into new redshift regimes using the *JWST*/NIRCam F466N and F470N filters. Simultaneously, JELS aims to provide a window into the resolved properties of star-forming galaxies at cosmic noon with matching F212N and F200W observations. The JELS Cycle 1 observations presented cover $\sim 63\text{ arcmin}^2$ within the wider PRIMER COSMOS legacy field (Dunlop et al., *in prep.*), which provides both the key F444W broadband imaging necessary for F466N/F470N excess selection as well as extensive multi-wavelength imaging required for robust line identification.

We have demonstrated that the JELS imaging reaches the extremely high sensitivities required to achieve the survey’s primary science goals. Based on the distribution of 5σ limiting magnitudes in the F466N and F470N mosaics (in 0.3 arcsec diameter apertures), the limiting line fluxes are estimated to be $1\text{--}1.6 \times 10^{-18}\text{ erg s}^{-1}\text{cm}^{-2}$ over 90 per cent of the field, reaching up to $\sim 2\times$ fainter emission lines than current slitless spectroscopic surveys in the literature. For the primary science goal of probing $H\alpha$ at $z \sim 6.1$, these flux limits correspond to $\log_{10}(L_{H\alpha}/\text{erg s}^{-1}) \sim 41.69\text{--}41.85$, or unobscured star-formation rates of $1\text{--}1.6\text{ M}_{\odot}\text{ yr}^{-1}$.

The preliminary F212N narrow-band mosaic reaches line sensitivities of $1.8\text{--}2.9 \times 10^{-18}\text{ erg s}^{-1}\text{cm}^{-2}$, corresponding to $\log_{10}(L_{H\alpha}/\text{erg s}^{-1}) \sim 40.85\text{--}41.05$; a factor of $\sim 5\text{--}10$ further down the $z = 2.23\text{ H}\alpha$ LF than previously available from ground-based narrow-band surveys. The combination of this extraordinary depth with *JWST*’s exquisite spatial resolution offers an unprece-

dent view of the resolved star-formation properties in galaxies at the peak of cosmic star formation history, for example by enabling detailed morphological comparison between $H\alpha$, UV and in-situ stellar mass in representative samples of galaxies.

We have highlighted the unique science cases for the JELS observations: a census of $H\alpha$ emitters at $z \sim 6.1$ that offers complementary constraints on the cosmic star-formation history and the galaxy population in the early Universe, novel probes of both early (through $[O\text{ III}]$ emitters) and late stages ($H\alpha$ at $z \sim 6.1$) of cosmic reionization, dust unbiased samples of star-forming galaxies at cosmic noon ($H\alpha/\text{Pa}\alpha/\text{Pa}\beta$), and spatially resolved properties of ionised gas in galaxies on sub-kpc scales at $2 < z < 6$. Initial results for the primary $H\alpha$ sample at $z \sim 6.1$ are presented in a companion paper, Pirie et al. (2024), with a number of further studies on the detailed properties of $H\alpha$, $\text{Pa}\alpha/\text{Pa}\beta$ and $[O\text{ III}]$ samples also in progress. With JELS adding both novel wavelength information (F212N, F466N, F470N) and significant additional broadband sensitivity (F200W) within one of the key extra-galactic legacy fields, we expect the broader scientific return from the community to extend far beyond these initial goals.

ACKNOWLEDGEMENTS

The authors thank David Coulter and Armin Rest for allowing the inclusion of JELS targets in their director’s discretionary observing programme. KJD acknowledges support from the Science and Technology Facilities Council (STFC) through an Ernest Rutherford Fellowship (grant number ST/W003120/1). DJM, PNB, RK and RJM acknowledge the support of the UK STFC via grant ST/V000594/1. PNB is grateful for support from the UK STFC via grant ST/Y000951/1. RKC was funded by support for program #02321, provided by NASA through a grant from the Space Telescope Science Institute, which is operated by the Association of

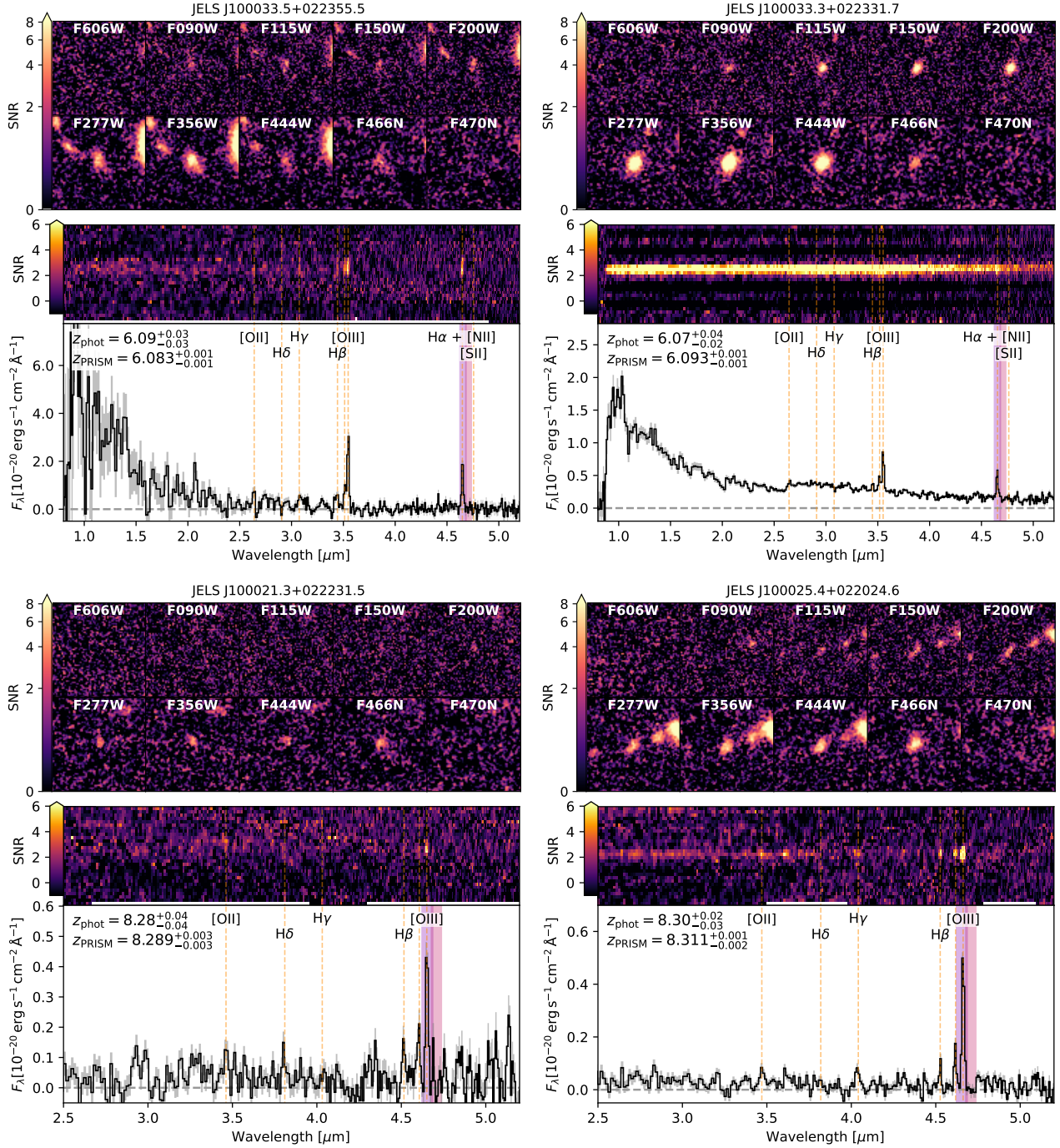


Figure 8. Example emission-line sources selected in JELS narrow-band imaging with spectroscopic confirmation from NIRSpect PRISM spectroscopy (DD 6585, PI Coulter). For each source, the upper panel shows photometry cutouts ($2 \text{ arcsec} \times 2 \text{ arcsec}$) from HST/ACS (F606W) and JWST/NIRCam from both PRIMER and JELS. The lower panel for each source shows the corresponding standard pipeline reduced 2D and 1D PRISM spectra. A subset of bright rest-frame optical emission lines at the confirmed spectroscopic redshift are illustrated by the vertical dashed lines and corresponding labels. Shaded regions also show the wavelength coverage of the overlapping F466N and F470N filters for reference. The top row shows sources selected as $H\alpha$ emitters, while the bottom row shows sources selected as robust $z \sim 8.3$ $[\text{O III}]\lambda 5008$ emitters. Note that at $z \sim 8.3$, the width of the F466N/F470N narrow-bands is such that $[\text{O III}]\lambda 5008$ and $[\text{O III}]\lambda 5008$ (and potentially $H\beta$) can be individually isolated from photometry alone.

Universities for Research in Astronomy, Inc., under NASA contract NAS5-03127. RKC is grateful for support from the Leverhulme Trust via the Leverhulme Early Career Fellowship. JSD acknowledges the support of the Royal Society via a Royal Society Research Professorship. CLH acknowledges support from the Leverhulme Trust through

an Early Career Research Fellowship and also acknowledge support from the Oxford Hintze Centre for Astrophysical Surveys which is funded through generous support from the Hintze Family Charitable Foundation. E.I. acknowledges funding by ANID FONDECYT Regular 1221846. AMS and IRS acknowledge support from the STFC

via grant ST/X001075/1. This work was initiated in part at Aspen Center for Physics, which is supported by National Science Foundation grant PHY-2210452. For the purpose of open access, the author has applied a Creative Commons Attribution (CC BY) licence to any Author Accepted Manuscript version arising from this submission.

DATA AVAILABILITY

The data underlying this article are available in the Mikulski Archives for Space Telescopes (MAST) Portal under proposal ID numbers 2321 (JELS imaging) and 6585 (NIRSpec PRISM spectroscopy). Higher level data products, including reduced mosaics in the JELS narrow and broadband filters, as well as associated catalogues will be made publicly available upon acceptance of this article and the associated publication (Pirie et al. 2024). Any other data produced for the article will be shared on reasonable request to the corresponding author.

REFERENCES

- Arellano-Córdova K. Z., et al., 2022, *ApJ*, 940, L23
- Arrabal Haro P., et al., 2023, *Nature*, 622, 707
- Bacon R., et al., 2010, in McLean I. S., Ramsay S. K., Takami H., eds, Society of Photo-Optical Instrumentation Engineers (SPIE) Conference Series Vol. 7735, Ground-based and Airborne Instrumentation for Astronomy III. p. 773508, doi:10.1117/12.856027
- Bhatawdekar R., Conselice C. J., Margalef-Bentabol B., Duncan K., 2019, *MNRAS*, 486, 3805
- Bouwens R. J., Illingworth G., Ellis R. S., Oesch P., Stefanon M., 2022, *ApJ*, 940, 55
- Brammer G. B., van Dokkum P. G., Coppi P., 2008, *ApJ*, 686, 1503
- Bunker A. J., et al., 2023, arXiv e-prints, p. arXiv:2306.02467
- Cameron A. J., et al., 2023, *A&A*, 677, A115
- Carniani S., et al., 2024, *Nature*, 633, 318
- Cheng C., et al., 2020, *MNRAS*, 499, 5241
- Clarke C., Oey M. S., 2002, *MNRAS*, 337, 1299
- Cleri N. J., et al., 2022, *ApJ*, 929, 3
- Cochrane R. K., Best P. N., Sobral D., Smail I., Wake D. A., Stott J. P., Geach J. E., 2017, *MNRAS*, 469, 2913
- Cochrane R. K., Best P. N., Sobral D., Smail I., Geach J. E., Stott J. P., Wake D. A., 2018, *MNRAS*, 475, 3730
- Cochrane R. K., et al., 2021, *MNRAS*, 503, 2622
- Cochrane R. K., et al., 2023, *MNRAS*, 523, 2409
- Conselice C. J., et al., 2024, *MNRAS*, 531, 4857
- Covelo-Paz A., et al., 2024, arXiv e-prints, p. arXiv:2409.17241
- Curti M., et al., 2023, *MNRAS*, 518, 425
- Curtis-Lake E., et al., 2023, *Nature Astronomy*, 7, 622
- De Barros S., Oesch P. A., Labbé I., Stefanon M., González V., Smit R., Bouwens R. J., Illingworth G. D., 2019, *MNRAS*, 489, 2355
- Donnan C. T., et al., 2024, *MNRAS*, 533, 3222
- Dudzevičiūtė U., et al., 2020, *MNRAS*, 494, 3828
- Duncan K. J., et al., 2019, *A&A*, 622, A3
- Endsley R., Stark D. P., Whittler L., Topping M. W., Chen Z., Plat A., Chisholm J., Charlot S., 2023, *MNRAS*, 524, 2312
- Estrada-Carpenter V., et al., 2024, *MNRAS*, 532, 577
- Ferreira L., et al., 2022, *ApJ*, 938, L2
- Flury S. R., et al., 2022, *ApJ*, 930, 126
- Flury S. R., et al., 2024, arXiv e-prints, p. arXiv:2409.12118
- Gaia Collaboration et al., 2022, arXiv e-prints, p. <https://arxiv.org/abs/2208.00211>
- Geach J. E., Smail I., Best P. N., Kurk J., Casali M., Ivison R. J., Coppin K., 2008, *MNRAS*, 388, 1473
- Geach J. E., Sobral D., Hickox R. C., Wake D. A., Smail I., Best P. N., Baugh C. M., Stott J. P., 2012, *MNRAS*, 426, 679
- de Graaff A., et al., 2024, arXiv e-prints, p. arXiv:2409.05948
- Greene J. E., et al., 2024, *ApJ*, 964, 39
- Grogin N. A., et al., 2011, *ApJS*, 197, 35
- Hao C.-N., Kennicutt R. C., Johnson B. D., Calzetti D., Dale D. A., Moustakas J., 2011, *ApJ*, 741, 124
- Harikane Y., et al., 2022, *ApJS*, 259, 20
- Hayes M., Schaerer D., Östlin G., 2010, *A&A*, 509, L5
- Hu W., et al., 2024, *ApJ*, 971, 21
- Isobe Y., et al., 2023, *ApJ*, 959, 100
- Jakobsen P., et al., 2022, *A&A*, 661, A80
- Kartaltepe J. S., et al., 2023, *ApJ*, 946, L15
- Kashino D., Lilly S. J., Matthee J., Eilers A.-C., Mackenzie R., Bordoloi R., Simcoe R. A., 2023, *ApJ*, 950, 66
- Khostovan A. A., Sobral D., Mobasher B., Smail I., Darvish B., Nayyeri H., Hemmati S., Stott J. P., 2016, *MNRAS*, 463, 2363
- Killi M., et al., 2023, arXiv e-prints, p. arXiv:2312.03065
- Koekemoer A. M., et al., 2011, *ApJS*, 197, 36
- Labbe I., et al., 2023, arXiv e-prints, p. arXiv:2306.07320
- Larson R. L., et al., 2023a, *ApJ*, 953, L29
- Larson R. L., et al., 2023b, *ApJ*, 958, 141
- Liu Z., Morishita T., Kodama T., 2024, arXiv e-prints, p. arXiv:2406.11188
- Madau P., Dickinson M., 2014, *ARA&A*, 52, 415
- Maiolino R., et al., 2023, arXiv e-prints, p. arXiv:2308.01230
- Mascia S., et al., 2024, *A&A*, 685, A3
- Maseda M. V., et al., 2023, *ApJ*, 956, 11
- Maseda M. V., et al., 2024, *A&A*, 689, A73
- Mason C. A., Treu T., Dijkstra M., Mesinger A., Trenti M., Pentericci L., de Barros S., Vanzella E., 2018, *ApJ*, 856, 2
- Matharu J., et al., 2024, arXiv e-prints, p. arXiv:2404.17629
- Matthee J., Sobral D., Best P., Smail I., Bian F., Darvish B., Röttgering H., Fan X., 2017, *MNRAS*, 471, 629
- Matthee J., Mackenzie R., Simcoe R. A., Kashino D., Lilly S. J., Bordoloi R., Eilers A.-C., 2023, *ApJ*, 950, 67
- Matthee J., et al., 2024, *ApJ*, 963, 129
- Meyer R. A., et al., 2024, arXiv e-prints, p. arXiv:2405.05111
- Mortlock A., et al., 2013, *MNRAS*, 433, 1185
- Mármol-Queraltó E., McLure R. J., Cullen F., Dunlop J. S., Fontana A., McLeod D. J., 2016, *MNRAS*, 460, 3587
- Nelson E. J., et al., 2013, *ApJ*, 763, L16
- Nelson E. J., et al., 2016, *ApJ*, 828, 27
- Oesch P. A., et al., 2023, *MNRAS*, 525, 2864
- Oke J. B., Gunn J. E., 1983, *ApJ*, 266, 713
- Parsa S., Dunlop J. S., McLure R. J., Mortlock A., 2016, *MNRAS*, 456, 3194
- Pirie C. A., et al., 2024, arXiv e-prints, p. arXiv:2410.11808
- Pirzkal N., et al., 2018, *ApJ*, 868, 61
- Pirzkal N., et al., 2024, *ApJ*, 969, 90
- Prieto-Lyon G., et al., 2023, *A&A*, 672, A186
- Reddy N. A., et al., 2018, *ApJ*, 869, 92
- Rieke M. J., Kelly D., Horner S., 2005, in Heaney J. B., Burriesci L. G., eds, Society of Photo-Optical Instrumentation Engineers (SPIE) Conference Series Vol. 5904, Cryogenic Optical Systems and Instruments XI. pp 1–8, doi:10.1117/12.615554
- Rieke M. J., et al., 2023, *PASP*, 135, 028001
- Rigby J., et al., 2023, *PASP*, 135, 048001
- Robertson B., et al., 2024, *ApJ*, 970, 31
- Robotham A. S. G., D’Silva J. C. J., Windhorst R. A., Jansen R. A., Summers J., Driver S. P., Wilmer C. N. A., Bellstedt S., 2023, *PASP*, 135, 085003
- Roy N., et al., 2023, *ApJ*, 952, L14
- Sanders R. L., Shapley A. E., Topping M. W., Reddy N. A., Brammer G. B., 2023, *ApJ*, 955, 54
- Saxena A., et al., 2024, *A&A*, 684, A84
- Scarлата C., Hayes M., Panagia N., Mehta V., Haardt F., Bagley M., 2024, arXiv e-prints, p. arXiv:2404.09015
- Shapley A. E., Reddy N. A., Sanders R. L., Topping M. W., Brammer G. B., 2023, *ApJ*, 950, L1
- Shen L., et al., 2024, *ApJ*, 963, L49
- Simmonds C., et al., 2023, *MNRAS*, 523, 5468
- Simmonds C., et al., 2024, arXiv e-prints, p. arXiv:2409.01286

- Smith A., Ma X., Bromm V., Finkelstein S. L., Hopkins P. F., Faucher-Giguère C.-A., Kereš D., 2018, *MNRAS*, 484, 39
- Sobral D., et al., 2009, *MNRAS*, 398, 75
- Sobral D., Best P. N., Geach J. E., Smail I., Cirasuolo M., Garn T., Dalton G. B., Kurk J., 2010, *MNRAS*, 404, 1551
- Sobral D., Best P. N., Smail I., Geach J. E., Cirasuolo M., Garn T., Dalton G. B., 2011, *MNRAS*, 411, 675
- Sobral D., Smail I., Best P. N., Geach J. E., Matsuda Y., Stott J. P., Cirasuolo M., Kurk J., 2012, *MNRAS*, 428, 1128
- Sobral D., Smail I., Best P. N., Geach J. E., Matsuda Y., Stott J. P., Cirasuolo M., Kurk J., 2013, *MNRAS*, 428, 1128
- Sobral D., Kohn S. A., Best P. N., Smail I., Harrison C. M., Stott J., Calhau J., Matthee J., 2016, *MNRAS*, 457, 1739
- Somerville R. S., Davé R., 2015, *ARA&A*, 53, 51
- Stark D. P., Ellis R. S., Chiu K., Ouchi M., Bunker A., 2010, *MNRAS*, 408, 1628
- Storey P. J., Hummer D. G., 1995, *MNRAS*, 272, 41
- Storey P. J., Zeppen C. J., 2000, *MNRAS*, 312, 813
- Stott J. P., et al., 2014, *MNRAS*, 443, 2695
- Sun G., Faucher-Giguère C.-A., Hayward C. C., Shen X., 2023a, *MNRAS*, 526, 2665
- Sun G., Faucher-Giguère C.-A., Hayward C. C., Shen X., Wetzel A., Cochrane R. K., 2023b, *ApJ*, 955, L35
- Swinbank M., et al., 2012, *The Messenger*, 149, 40
- Tang M., et al., 2023, *MNRAS*, 526, 1657
- Theios R. L., Steidel C. C., Strom A. L., Rudie G. C., Trainor R. F., Reddy N. A., 2019, *ApJ*, 871, 128
- Topping M. W., et al., 2024, *MNRAS*, 529, 3301
- Umeda H., Ouchi M., Nakajima K., Harikane Y., Ono Y., Xu Y., Isobe Y., Zhang Y., 2024, *ApJ*, 971, 124
- Urrutia T., et al., 2019, *A&A*, 624, A141
- Witstok J., et al., 2024, *A&A*, 682, A40
- Yung L. Y. A., Somerville R. S., Popping G., Finkelstein S. L., Ferguson H. C., Davé R., 2019, *MNRAS*, 490, 2855

This paper has been typeset from a $\text{\TeX}/\text{\LaTeX}$ file prepared by the author.